Research Square

Preprints are preliminary reports that have not undergone peer review.
They should not be considered conclusive, used to inform clinical practice,
or referenced by the media as validated information.

A Cable Partial Discharge Denoising Method Based on RIME-VMD-IWT

Ke Shang
State Grid Beijing Shunyi Electric Power Company
Jianwei Song
State Grid Beijing Shunyi Electric Power Company
Yikang He
yk23691@126.com

State Grid Beijing Shunyi Electric Power Company
Lan Su
Tsinghua Sichuan Energy Internet Research Institute
Lele Liu
State Grid Beijing Shunyi Electric Power Company
Xiao Liu
State Grid Beijing Shunyi Electric Power Company
Yunpeng Wang
State Grid Beijing Shunyi Electric Power Company

Research Article

Keywords:

Posted Date: November 18th, 2026

DOI: https://doi.org/10.21203/rs.3.rs-10161442/v1

License: This work is licensed under a Creative Commons Attribution 4.0 International License.
Read Full License

Additional Declarations: No competing interests reported.

A Cable Partial Discharge Denoising Method Based on RIME-VMD-IWT

Ke Shang[1], Jianwei Song[1], Yikang He[1]*, Lan Su[2], Lele Liu[1], Xiao Liu[1], Yunpeng Wang[1]
(1. State Grid Beijing Shunyi Electric Power Company, Beijing 101399;
2. Tsinghua Sichuan Energy Internet Research Institute, Chengdu 610213)

Abstract: Among the various online monitoring methods for assessing the insulation condition of high-voltage cables, partial discharge (PD) detection is among the most widely applied. However, PD signals acquired in field environments are highly susceptible to noise interference. To address this issue, this paper proposes a PD signal denoising method that integrates the Rime Optimization Algorithm (RIME) with Variational Mode Decomposition (VMD) and Improved Wavelet Threshold (IWT) denoising. First, the RIME algorithm adaptively optimizes the number of modes K and the penalty factor α in VMD. The optimized VMD then decomposes the noisy PD signal into K intrinsic mode functions (IMFs), and the Composite Multiscale Fuzzy Dispersion Entropy (CMFDE) is introduced to characterize each IMF, thereby distinguishing effective signal components from noise components. Finally, IWT is applied to the effective components for secondary denoising to suppress residual noise and reconstruct the denoised PD signal. Simulation experiments and field-measured data demonstrate that the proposed method effectively removes noise interference in high-voltage cable PD signals and significantly improves the signal-to-noise ratio and reconstruction accuracy, enabling accurate online monitoring of high-voltage cable insulation condition.

Keywords: partial discharge; variational mode decomposition; rime-ice optimization algorithm; composite multiscale fuzzy dispersion entropy; improved wavelet threshold denoising

1 Introduction

Cross-linked polyethylene (XLPE) cables are widely used in power supply systems owing to their excellent insulation performance. However, during long-term operation, partial discharge (PD) may occur within the cable as a result of aging, external mechanical damage, moisture ingress, and other factors[1–5]. Accurately interpreting and identifying PD signals has therefore become a core technical aspect of PD online monitoring systems[6].

Real-time online monitoring of high-voltage cables is a key factor in ensuring their reliable operation. However, the substantial noise present in actual field environments makes it difficult to accurately capture the PD signal; denoising the noisy PD signal is therefore a critical issue at present. References [7–8] employ Empirical Mode Decomposition (EMD) for signal processing. Although EMD achieves a certain denoising effect, its inherent mode mixing and end effects leave the denoising incomplete. Reference [9] applies the Wavelet Transform (WT) for denoising; while this method effectively suppresses white noise, the denoising result is highly sensitive to the choice of wavelet threshold, and its ability to suppress periodic narrowband interference is limited. Reference [10] proposes a denoising strategy based on Singular Value Decomposition (SVD), which distinguishes effective signal components from noise components by setting a singular-value threshold. This approach performs well in suppressing periodic narrowband interference, but its white-noise removal is unsatisfactory. Variational Mode Decomposition (VMD) can overcome the mode-mixing problem of traditional decomposition methods, but its decomposition quality depends heavily on two key parameters: the number of modes K and the quadratic penalty factor α. Specifically, K determines the number of decomposed modes, which directly affects the completeness of signal feature extraction, whereas α controls the bandwidth of each mode component, thereby influencing the decomposition accuracy and noise robustness. To optimize the selection of K and α, researchers have proposed various intelligent optimization algorithms, such as the Pelican Optimization Algorithm (POA)[11] and the Whale Optimization Algorithm (WOA)[12]. However, these algorithms generally tend to fall into local optima and suffer from

slow convergence and insufficient optimization accuracy, which limit the application of VMD in practical engineering.

To address the above problems, this paper proposes a PD signal denoising method based on RIME-VMD-IWT. First, the RIME algorithm [13] is employed to adaptively optimize the number of modes K and the penalty factor α of VMD. The optimized VMD then decomposes the noisy PD signal into several intrinsic mode functions (IMFs), and the Composite Multiscale Fuzzy Dispersion Entropy (CMFDE) [14–15] is introduced to characterize each IMF, thereby distinguishing effective signal components from noise components. Finally, the effective components undergo secondary denoising via the Improved Wavelet Thresholding (IWT) method to suppress residual noise and yield the denoised PD signal. Simulation and field-measured data show that the proposed method outperforms conventional methods in both noise suppression and feature preservation, and provides a reliable signal-processing basis for online monitoring of high-voltage cable insulation condition.

2 Signal Denoising Method Based on RIME-VMD-IWT

The overall structure of the proposed RIME-VMD-IWT-based PD signal denoising method is shown in Fig. 1. The specific steps are as follows: first, the RIME algorithm is used to adaptively optimize the number of modes K and the penalty factor α in VMD; second, the optimized VMD is used to decompose the noisy PD signal into multiple IMFs, and CMFDE is used to discriminate the properties of each IMF component so as to distinguish effective signal components from noise components; finally, IWT is applied to the effective signal components for secondary denoising to remove residual noise, and the denoised PD signal is obtained after the noise components are eliminated. The detailed execution flow of this denoising method is shown in Fig. 2.

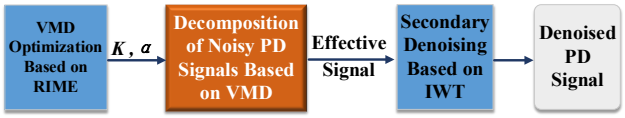


Fig. 1 The proposed RIME-VMD-IWT-based PD denoising method

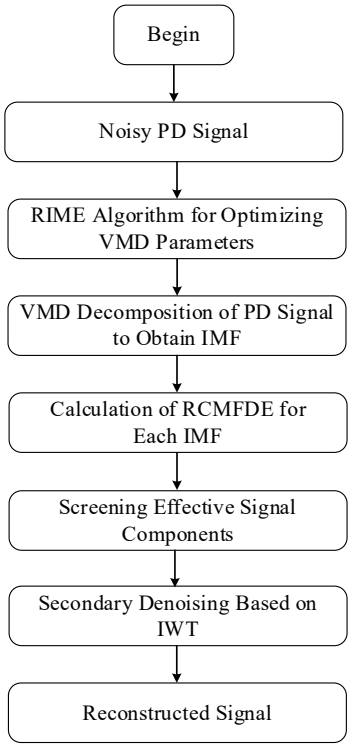


Fig. 2 The flow of the proposed denoising method

2.1 VMD Optimization Based on RIME

By optimizing the mode variational model, VMD can adaptively obtain the center frequency and bandwidth of each mode component, thereby completing effective signal decomposition and denoising[11]. However, its denoising effect depends heavily on the proper selection of the two parameters K and α, because they directly affect the number of mode components and their bandwidth constraints, and thus play a key role in the denoising result of the PD signal. Compared with similar optimization methods, the RIME algorithm has two complementary iterative search strategies, which achieve a good balance between exploring unknown regions and exploiting known information. This algorithm can effectively avoid falling into local optima and can find suitable values of K and α, enabling VMD to decompose the signal accurately.

The RIME algorithm is a novel optimization method inspired by the rime-ice formation process, proposed in research published in 2023 by Su Hang[13]. By simulating the different growth characteristics of soft rime and hard rime, the algorithm designs a corresponding soft-rime search strategy and a hard-rime puncture mechanism, thereby achieving a coordinated unity of global exploration and local exploitation during optimization.-rime search strategy and the hard-rime puncture mechanism, thereby achieving a coordinated unity of

global exploration and local exploitation during the optimization process.

2.1.1 Soft-rime Search Mechanism

During the iterative updating of the RIME algorithm, each rime particle moves according to established rules. For a free particle, when its motion trajectory brings it within the effective range of the soft-rime region, it aggregates and condenses with the particles already present in the soft-rime structure; conversely, if the particle's endpoint falls outside the effective radius of this region, the above combination does not occur. As the iteration proceeds, the whole system gradually reaches a stable state of dynamic equilibrium under the combined action of internal and external environmental conditions.

$$\left\{\begin{array}{c} R_{ij}^{new}=R_{best.j}+r_1\cdot\cos\theta\cdot\beta\cdot\left(h\cdot\left(Ub_{ij}-Lb_{ij}\right)+Lb_{ij}\right) \\ r_2<E \end{array}\right\} \quad (1)$$

where R_{ij}^{new} denotes the updated position of the particle, $R_{best.j}$ is the j-th particle of the best crystal in the rime population. The parameter r_1 is the global exploration factor, and r_1 controls the direction of particle movement and $\cos\theta$ changes with the number of iterations, β is the environmental factor, h is the adhesion degree, a random number in the range (0, 1) used to control the distance between the centers of two rime particles, Ub_{ij} and Lb_{ij} represents the upper and lower bounds of the particle's spatial motion.

2.1.2 Hard-rime Puncture Mechanism

In a strong-wind environment, because the wind is strong, the hard rime grows along the wind direction, and owing to this co-directional extension, different icecrystal structures easily overlap and penetrate one another; this phenomenon is defined as rime puncture.

Based on the rime-puncture mechanism, the algorithm allows ordinary particles and the current best particle to exchange information across some dimensions. This strategy not only helps accelerate convergence but also enhances the optimization performance of the algorithm over the whole solution space. The update formula for the hard-rime position is:

$$R_{ij}^{new}=R_{best.j},r_3<F^{\mathrm{nomr}}\left(S_i\right) \quad (2)$$

where $F^{\mathrm{nomr}}\left(S_i\right)$ denotes the normalized value of the fitness of the i-th agent, denotes the probability that the i-th particle is selected, r_3 is a random number in the range (0,1). R_{ij}^{new} denotes the updated position of the particle, $R_{best.j}$ is the j-th particle of the best crystal in the rime population.

When the RIME algorithm is employed to jointly optimize the two VMD parameters K and α, an appropriate fitness function must be constructed to guide the search. If the preset number of modes K is too small, the different frequency components of the original signal cannot be fully separated, leading to incomplete decomposition: components from different frequency bands become mixed within a single mode, resulting in mode mixing and degrading the accuracy of subsequent analysis. Conversely, if K is too large, over-decomposition occurs, generating spurious components that contain substantial noise and compromising the fidelity of the reconstructed signal. The parameter α mainly adjusts the bandwidth constraint of the mode components: an excessively small α makes the bandwidth too wide, so that noise cannot be effectively separated and suppressed, whereas an excessively large α makes the bandwidth too narrow, potentially filtering out useful signal components and causing loss of effective information.

To select the best objective function among the Center Frequency Variance (CFV), Permutation Entropy (PE) and Minimum Envelope Entropy (Min-EE), the best-performing objective function, this paper uses two indices, the Modal Aliasing Index (MAI) and the Effective Mode Number (EMN), to evaluate the decomposition effect; the detailed results are given in Table 1. MAI quantifies the area proportion of the mode-mixing region: the lower the value, the milder the mode mixing and the higher the purity of the decomposition; EMN characterizes the number of effective modes retained after decomposition: the larger the value, the richer the decomposed mode components and the finer the description of the original information.

Table 1 Decomposition effects of different objective functions

Objective function	Optimization parameters(K,α)	EMN	MAI/%
CFV	(6,2100)	2	9.6
Min-EE	(5,1800)	4	8.2
PE	(7,2300)	3	10.4

As can be seen from Table 1, when the objective function is Min-EE, MAI is the smallest and EMN is the largest, so selecting Min-EE as the objective function

gives the best effect. The envelope entropy $IMF_j(j)(j=1,2\cdots N)$ of the signal H_p is calculated as:

$$H_p = -\sum_{j=1}^{N} p_{i,j} \lg p_{i,j} \tag{3}$$

where

$$p_{i,j} = \frac{\alpha(j)}{\sum_{j=1}^{N} \alpha_i(j)} \tag{4}$$

where i is the index of the IMF obtained by decomposing the original signal; $\alpha_i(j)$ denotes the envelope signal $IMF_i(j)$ obtained after *Hilbert* transforming the signal; $p_{i,j}$ is $\alpha_i(j)$ the normalized form of. The detailed flow of RIME optimizing VMD is shown in Fig. 3.

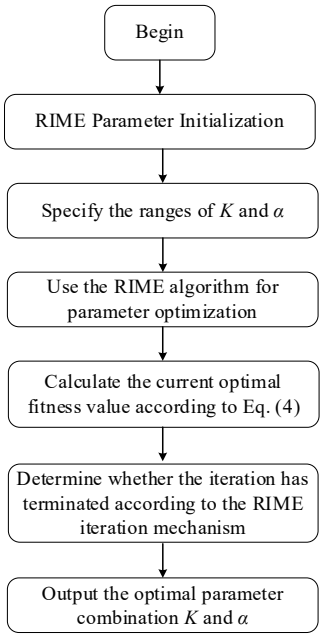


Fig. 3 Flow of the RIME-VMD algorithm

2.2 Noisy PD Signal Decomposition Based on VMD

VMD is a signal-processing method built on a rigorous mathematical framework. Its core idea is to decompose the original signal into several IMFs, each with a specific center frequency and a limited bandwidth. These IMFs correspond to the signal components in different frequency bands, and the optimal center frequency and bandwidth of each IMF are determined adaptively through a variational optimization model. By virtue of this property, VMD can effectively separate a noisy PD signal into effective signal components and noise components. The VMD model is expressed by Eq. (5):

$$\begin{aligned} L(\{u_k\},\{\omega_k\},\{\lambda\}) = \\ \alpha\sum_{k=1}^{K}\left\|\partial_t\left[\left(\delta(t)+\frac{j}{\pi t}\right)u_k(t)\right]e^{-j\omega_k t}\right\|_2^2 \\ +\left\|f(t)-\sum_{k=1}^{K}u_k(t)\right\|_2^2+\left\langle\lambda(t),f(t)-\sum_{k=1}^{K}u_k(t)\right\rangle \end{aligned} \tag{5}$$

where K is the number of modes to be decomposed, $\{u_k\}$ is the k-th mode component after decomposition, $\{\omega_k\}$ is the center frequency, $\delta(t)$ is the impulse function, λ is the Lagrange multiplier operator, and α is the quadratic penalty factor.

To distinguish the effective signal from the noise signal in the IMFs, this paper uses CMFDE to discriminate the properties of each IMF component. Fuzzy Dispersion Entropy (FDE) is a tool for measuring sequence complexity[16]; it uses a fuzzy membership function to replace the rounding mapping mechanism of traditional dispersion entropy, effectively reducing the entropy fluctuation caused by weak disturbances in the sequence and improving the robustness to signal features. However, FDE still suffers from information loss in the mapping step, and analysis at a single scale cannot fully capture the multi-level structural features of the signal. To solve this problem, this paper adopts the CMFDE method[17], which, through multiscale analysis, can obtain a more comprehensive feature representation from the signal, thereby effectively improving the accuracy of entropy calculation and the reliability of IMF-component classification. CMFDE method is computed as follows:

The sequence $x=\{x_1,x_2,x_3,\ldots x_N\}$ is obtained through the normal distribution function:

$$y_i = \frac{1}{\delta\sqrt{2\pi}}\int_{-\infty}^{x_j} e^{\frac{-(t-\mu)^2}{2\sigma^2}}dt \tag{6}$$

where μ and σ^2 denote the expectation and variance.

Fuzzy dispersion entropy then sets the fuzzy membership based on the Euclidean distance:

$$z_i^c = round(c\cdot y_i + 0.5) \tag{7}$$

where, c denotes the number of the time series z^c, z_i^c denotes z^c the i-th member of. *round* is the rounding function.

Define the embedding vector:

$$d(i) = z(i:i+(m-1)\times d)\ i=1:N-(m-1)\times d \tag{8}$$

where m is the embedding dimension, d is the time delay.

If the embedding vector $z(i:i+(m-1)\times d)$ contains k dispersion patterns whose Euclidean distances are

smaller than the threshold r, with the corresponding distance matrix $dis(k)$, then the probability of each dispersion pattern is given by:

$$p\left(\pi_{v_0v_1\ldots v_{m-1}}\right)_{z(i:i+(m-1)\times d)}=\frac{r-dis(i)}{k\times r-sum(dis)} \tag{9}$$

Fuzzy dispersion entropy is defined as:

$$FuzzyDispEn(x,m,c,d)= -\sum_{\pi=1}^{c^m}p\left(\pi_{v_0v_1\ldots v_{m-1}}\right)\times\ln\left(p\left(\pi_{v_0v_1\ldots v_{m-1}}\right)\right) \tag{10}$$

For a time series of length N $x=[x_1,x_2,\ldots,x_N]$, a scale factor is introduced s; for each scale factor s, a sliding window generates s coarse-grained sequences. Each coarse-grained sequence is obtained by Eq. (11).

$$y_{k,j}^{s}=\frac{1}{s}\sum_{i=(j-1)s+k}^{js+k-1}x_i \tag{11}$$

where j denotes the window starting offset, $1\le j\le s$, k denotes, under a fixed scale factor s and starting offset j, the k-th sub-sequence obtained after segmenting the original time series.

For each scale factor s, the multiscale fuzzy dispersion entropy is computed as follows:

$$CMFDE(X,m,c,d,s)=\frac{1}{s}\sum_{k=1}^{s}FDE\left(y_k^s\right) \tag{12}$$

2.3 Secondary Denoising Based on IWT

To remove residual noise in the effective signal, this paper proposes the IWT method for noise suppression. The proposed IWT method improves the traditional WT method to systematically analyze the signal features at different decomposition levels. By setting different decomposition levels, the wavelet coefficients are processed hierarchically, and the threshold is dynamically adjusted according to the characteristics of each level, thereby enhancing the adaptivity of the method. This improvement helps to distinguish signal and noise components more accurately and reduces errors introduced by unreasonable classification of wavelet coefficients.

The traditional threshold formula and the improved threshold formula are shown in Eq. (13):

$$\left\{\begin{array}{l}\lambda=\delta\sqrt{2\ln N}\\ \lambda'=\dfrac{\delta\sqrt{2\ln N}}{\lg(n+1)}\end{array}\right\} \tag{13}$$

λ is the traditional threshold formula, λ' is the improved threshold formula, δ is the standard deviation of the signal, N is the total number of signal sampling points, n is the amplitude of the signal.

To eliminate the discontinuity of the traditional hard-threshold function at the threshold[14] and the constant bias of the traditional soft-threshold function[15], this paper proposes an improved threshold function, as shown in Eq. (14):

$$\omega_1'=\left\{\begin{array}{ll}\mathrm{sgn}(\omega_1)\left(|\omega_1|-\lambda'\left(1-e^{\frac{-\ln(b+1)}{|\omega_1|-\lambda'}}\right)e^{-\sqrt{\omega_1^2-\lambda'^2}}\right) & |\omega_1|\ge\lambda'\\ 0 & |\omega_1|\le\lambda'\end{array}\right. \tag{14}$$

where ω_1 is the wavelet coefficient; ω_1' is the thresholded wavelet coefficient, λ' is the improved threshold; sgn is the sign function, b is the adjustment parameter.

When $|\omega_1|\to\infty$, Eq. (15) is used to analyze the bias of the improved wavelet threshold function.

$$\left\{\begin{array}{l}\lim\limits_{x\to+\infty}(\omega_1'-\omega_1)=\omega_1-\lambda'\left(1-e^{\frac{-\ln(b+1)}{\omega_1-\lambda'}}\right)e^{-\sqrt{\omega_1^2-\lambda'^2}}-\omega_1=0\\ \lim\limits_{x\to-\infty}(\omega_1'-\omega_1)=\omega_1+\lambda'\left(1-e^{\frac{-\ln(b+1)}{-\omega_1-\lambda'}}\right)e^{-\sqrt{(-\omega_1)^2-\lambda'^2}}-\omega_1=0\end{array}\right. \tag{15}$$

From Eq. (15) it can be seen that the improved wavelet threshold function eliminates the constant bias of the traditional soft-threshold function.

$|\omega_1|\to\lambda'$, Eq. (16) is used to analyze the continuity of the improved wavelet threshold function.

$$\left\{\begin{array}{l}\lim\limits_{x\to+\lambda'}=\omega_1-\lambda'\left(1-e^{\frac{-\ln(b+1)}{\omega_1-\lambda'}}\right)e^{-\sqrt{\omega_1^2-\lambda'^2}}=0\\ \lim\limits_{x\to-\lambda'}=\omega_1+\lambda'\left(1-e^{\frac{-\ln(b+1)}{-\omega_1-\lambda'}}\right)e^{-\sqrt{(-\omega_1)^2-\lambda'^2}}=0\end{array}\right. \tag{16}$$

From Eq. (16) it can be seen that the improved wavelet threshold function eliminates the discontinuity of the traditional hard-threshold function.

It can thus be seen that the IWT methodeliminates the bias between the soft threshold and the original wavelet coefficients, while the adaptive threshold also resolves the discontinuity of the hard threshold.

3 Simulation Analysis

3.1 PD Signal Simulation

According to Reference [18], partial discharge signals in 10 kV high-voltage cables exhibit significant attenuation and oscillation characteristics during propagation. To verify the effectiveness of the proposed method, this paper selects the double-exponential decay

model and its oscillatory form to simulate the PD signal in an actual cable environment.where, the double-exponential decay model is expressed as follows:

$$f_{PD1}(t) = A_1\left(e^{-1.3t/\tau_1} - e^{-2.2t/\tau_1}\right) \quad (17)$$

the double-exponential decaying oscillation model is expressed as follows:

$$f_{PD2}(t) = A_2\left(e^{-1.3t/\tau_2} - e^{-2.2t/\tau_2}\right)\sin(2\pi f_b t) \quad (18)$$

In constructing the simulation signal, the mathematical expression of the partial discharge pulse involves several key parameters, set as follows: the two amplitude components A_1 and A_2 of the PD signal are set to 30 mV and 70 mV respectively to represent discharge pulses of different intensities; the oscillation frequency f_b is 10 MHz, and the decay coefficients τ_1 and τ_2 are both 40 40 us, used to control the decay rate of the pulse waveform. The sampling parameters of the signal are: number of sampling points N=2000 and sampling frequency is 50 MHz, to ensure the fineness of the time-domain waveform. The original noise-free PD signal waveform generated according to the above parameters is shown in Fig. 4. It can be seen that the simulated signal exhibits typical double-exponential decaying oscillation characteristics and can simulate the time-domain characteristics of partial discharge signals.

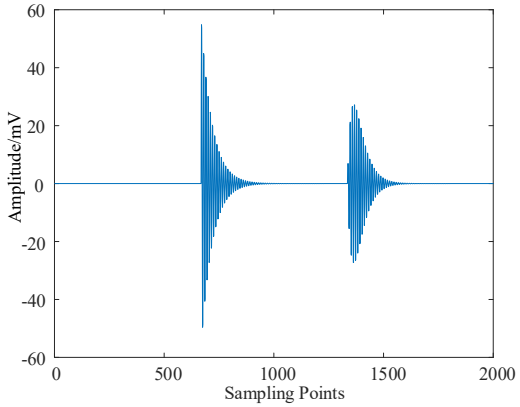


Fig. 4 Clean PD signal

Considering the typical noise components present at cable partial-discharge sites, white noise and periodic narrowband interference are introduced into the simulation signal; the resulting noisy PD signal is shown in Fig. 5. The periodic narrowband interference is represented by a periodic sinusoidal signal as: $z(t)$ is expressed as:

$$z(t) = B\sin(2\pi f_b t - \varphi) \quad (19)$$

The periodic narrowband interference parameters are listed in Table 2.

Table 2 Parameter settings

Narrowband interference	1	2	3	4	5
Amplitude/mV A_i /mV	2	2.5	3	3.5	4
Frequency/MHz f_i /MHz	0.3	0.5	0.8	1	1.5
Initial phase angle φ	π/12	π/9	π/6	π/4	π/2

After adding white noise and periodic narrowband interference noise, as shown in Fig. 5, the clean PDsignal is completely submerged in noise.

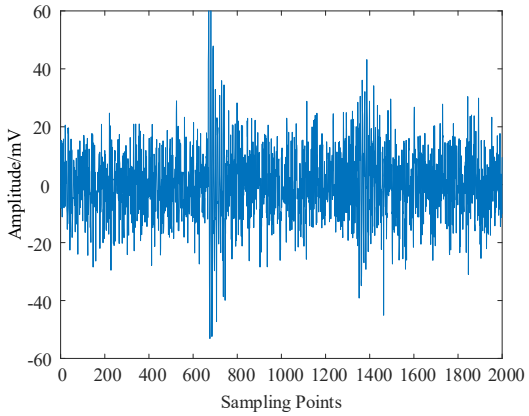


Fig. 5 Noisy PD signal

3.2 Denoising Evaluation Criteria

To evaluate the denoising performance of different methods and to facilitate comparison of their denoising effects, this study introduces the Signal-to-Noise Ratio (SNR), the Root Mean Square Error (RMSE) and the Normalized Correlation Coefficient (NCC) as quantitative indices, calculated as follows::

$$\mathrm{SNR}=10\lg\sum_{i=1}^{N}x_i^2 \Big/ \sum_{i=1}^{N}(y_i - x_i)^2 \quad (20)$$

$$\mathrm{RMSE}=\sqrt{\sum_{i=1}^{N}(x_i - y_i)^2 / N} \quad (21)$$

$$\mathrm{NCC}=\sum_{i=1}^{N}x_i y_i \Big/ \sqrt{(\sum_{i=1}^{N}x_i^2)(\sum_{i=1}^{N}y_i^2)} \quad (22)$$

where N is the number of sampling points, x_i denotes the clean signal, y_i denotes the denoised signal. To measure the denoising effect, SNR is usually used: the larger the value, the better the algorithm performs in suppressing noise. RMSE reflects the degree of deviation between the processed signal and the original reference signal: the lower the value, the smaller the signal distortion. NCC, by contrast, is used to evaluate the similarity of the waveforms: the closer this index is to 1, the better the reconstructed signal matches the original signal in waveform.

3.3 Comparison of PD Signal Denoising Methods

To verify the proposed RIME-VMD algorithm's superiority in parameter optimization, two optimization algorithms, WOA-VMD and POA-VMD, are selected for comparison experiments. The decomposition results of the three optimization algorithms on the noisy PD signal are shown in Figs. 6~8. As can be seen from Fig. 6, the signal decomposed by WOA-VMD still has many significant fluctuations, indicating that the noise components have not been effectively filtered out. This is mainly because the search strategy of the WOA algorithm in parameter optimization is relatively simple and cannot fully perform global exploration in the complex VMD parameter space.. In addition, the parameter-adjustment mechanism of this algorithm is relatively fixed, which affects the precise optimization of the number of modes K and the penalty factor α, ultimately limiting the decomposition effect.

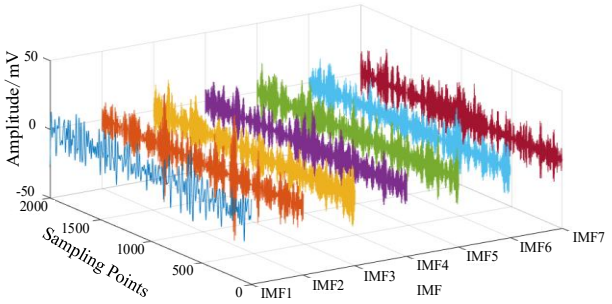


Fig. 6 WOA-VMD decomposition

As shown in Fig. 7, although the signal peak of POA-VMD is lower than that of WOA-VMD, the waveform still exhibits noticeable disorder and shows poor consistency with the original PD signal. These results indicate that POA-VMD has limited local-exploitation ability in complex multimodal optimization scenarios, which restricts its fine-grained search of the parameter space. As a result, it fails to achieve precise parameter optimization and cannot effectively separate noise from the effective signal during processing, thereby degrading the final denoising performance.

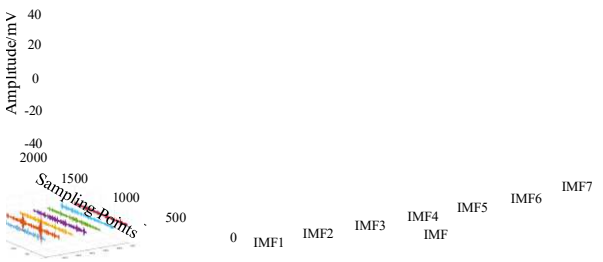


Fig. 7 POA-VMD decomposition

As shown in Fig. 8, the IMF components obtained by RIME-VMD decomposition exhibit small amplitude variations and maintain good mutual independence, which facilitates the subsequent reconstruction of the PD signal. This advantage stems from the dual mechanism of the soft-rime search strategy and the hard-rime puncture mechanism: in parameter optimization, the RIME algorithm achieves higher search efficiency and convergence accuracy and significantly enhances its ability to locate the optimal solution, thereby effectively balancing global exploration and local exploitation.

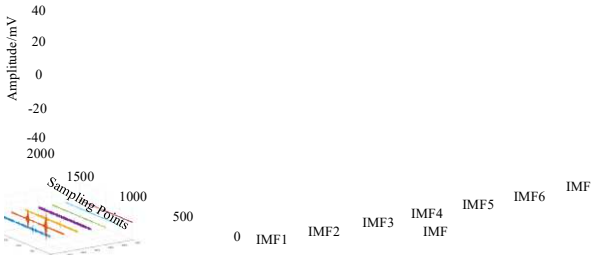


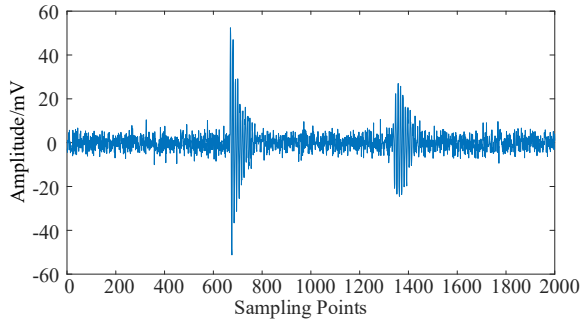
Fig. 8 RIME-VMD decomposition

A total of seven IMF components are obtained after RIME-VMD decomposition. To effectively distinguish effective signal components from noise components, the composite multiscale fuzzy dispersion entropy of each IMF is calculated, with the results shown in Table 3. As can be seen from Fig. 8 and Table 3, IMF1–IMF3 exhibit relatively regular waveforms with high consistency with the original signal and small CMFDE values, and are thus identified as PD-signal-dominant components, whereas IMF4–IMF7 show severe amplitude fluctuations, low consistency, and large CMFDE values, and are classified as noise-dominant components. Therefore, IMF1–IMF3 are retained as effective signal components, IMF4–IMF7 are discarded as noise-dominant components, and IWT is applied to perform secondary denoising on the retained components.

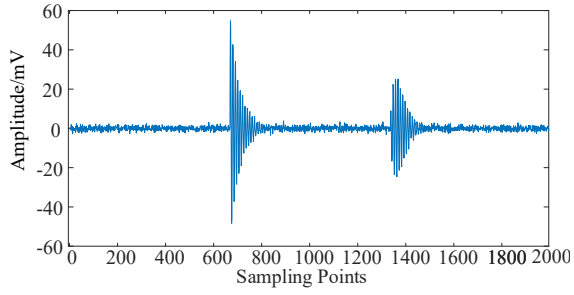
Table 3 RIME-VMDCMFDE of the IMFs obtained IMFby RIME-VMD decomposition

Component	CMFDE
IMF1	0.3945
IMF2	0.4028
IMF3	0.4203
IMF4	0.8534
IMF5	0.8639
IMF6	0.8725
IMF7	0.8826

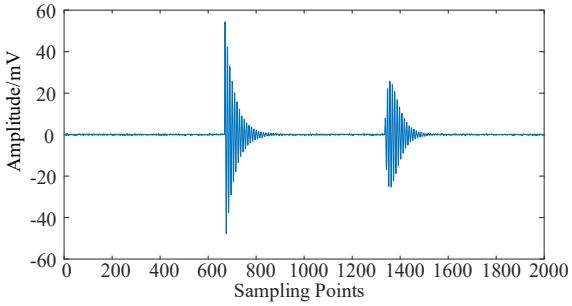
To comprehensively verify the effectiveness of the proposed denoising method, the WOA-VMD-WT, POA-VMD-WT, and proposed RIME-VMD-IWT methods are selected for comparison experiments. The denoising results of the three methods are shown in Fig. 9, and the quantitative performance indices are compared in Table 4. As shown in Fig. 9, the signals processed by the WOA-VMD-WT and POA-VMD-WT methods still contain considerable residual noise with large waveform fluctuations, indicating mediocre denoising performance. In contrast, after the noisy PD signal is processed by the proposed RIME-VMD-IWT method, the waveform becomes smooth and regular, with markedly improved consistency with the original PD signal, effectively preserving its main features; the denoising performance is clearly superior to that of the comparison methods. The data in Table 4 show that the signal denoised by the proposed method achieves an SNR of 112.3973 dB, significantly higher than those of the WOA-VMD-WT and POA-VMD-WT methods; an RMSE of 0.0736, clearly lower than those of the two comparison methods; and an NCC of 0.9578, the closest to 1, indicating the highest similarity between the denoised signal and the original PD signal. Together, these indices demonstrate that the proposed RIME-VMD-IWT method offers a clear advantage in denoising performance and can provide reliable technical support for online monitoring of PD signals.



(a)WOA-VMD-WT method



(b)POA-VMD-WT method



(c) proposedRIME-VMD-IWT method

Fig. 9 Denoising effects of different methods

Table 4 Evaluation parameters after denoising

Evaluation parameter	WOA-VMD-WT method	POA-VMD-WT method	the proposed RIME-VMD-IWT method
SNR	7.3837	5.2182	12.3973
RMSE	0.3751	0.2897	0.0736
NCC	0.6382	0.7335	0.9578

4 Field-Measured Analysis

To verify the practical performance of the proposed denoising method, a PD denoising test was conducted in the field, in which the noise background was constructed using the inherent environment and equipment. A Keysight 33600A series arbitrary waveform generator was employed to generate 1 MHz and 2 MHz sinusoidal signals to simulate periodic narrowband interference[19], and a broadband noise generator was used to output Gaussian white noise covering the frequency band from 100 kHz to 10 MHz [20]. A section of 10 kV high-voltage cable was selected, and an insulation defect was artificially introduced by clamping. For signal acquisition, a Rogowski-coil high-frequency current sensor installed on the cable grounding wire was used to couple the discharge pulses, and the waveforms were recorded by an oscilloscope and a host computer. The field experimental setup is shown in Fig. 10.

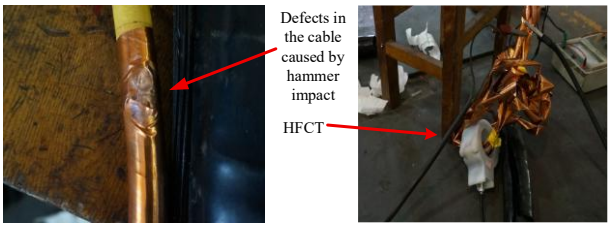


Fig. 10 Partial discharge experiment

Fig. 11 shows the acquired noisy PD signal waveform. As can be seen, under strong noise interference the PD

signal features are completely submerged in noise, the signal amplitude fluctuates violently, and it is difficult to directly identify the position and amplitude features of the partial discharge pulses.

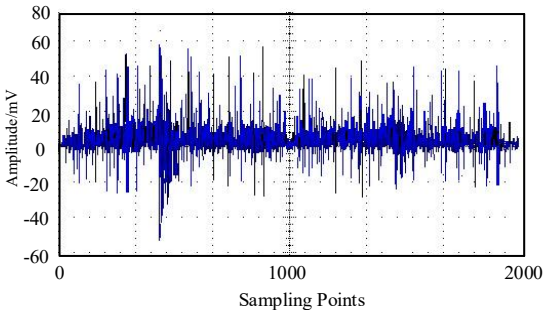
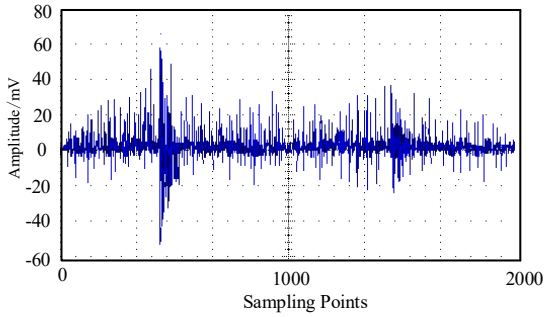
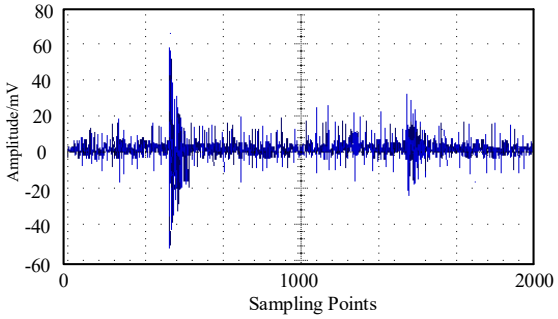


Fig. 11 Noisy PDsignal

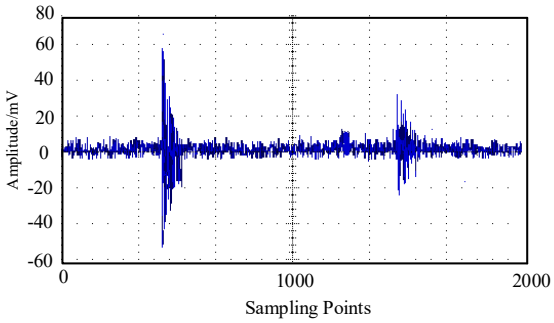
For the noisy PD signal shown in Fig. 11, the WOA-VMD-WT, POA-VMD-WT, and proposed RIME-VMD-IWT methods are used for denoising, and the experimental results are shown in Fig. 12. After processing with the WOA-VMD-WT method, the periodic narrowband interference and white-noise components remain relatively significant, with evident waveform fluctuations, indicating limited denoising performance. After processing with the POA-VMD-WT method, part of the noise is suppressed, but the identifiability of the PD features is reduced. In contrast, the signal processed by the proposed method matches the original PD signal more closely in waveform, with the PD pulse features well preserved, demonstrating a clear advantage in denoising performance.



(a)WOA-VMD-WT



(b)POA-VMD-WT



(c) Proposed RIME-VMD-IWT method

Fig. 12 Denoising effects on the measured PD signal

To evaluate the adaptability and robustness of the proposed method under noise interference of varying intensities, multiple simulated test environments with different input SNR values were constructed, and the performance of three typical denoising methods was compared to verify the overall advantage of the proposed method. The comparison results of the three methods under different SNR conditions are shown in Table 5. As can be seen from Table 5, the SNR of the signal processed by the proposed method is significantly higher than those of the other two methods, with a smaller root-mean-square error and a normalized correlation coefficient closest to 1. These results collectively indicate that the proposed method performs better in removing noise while retaining the useful signal, producing an output most consistent with the original signal.

Table 5 Comparison of denoising effects

Denoising method	Evaluation metric	SNR=-4	SNR=0	SNR=4
WOA-VMD-WT method	SNR	5.3483	5.8372	6.3736
	RMSE	0.3637	0.3527	0.2963
	NCC	0.7836	0.7936	0.8056
POA-VMD-WT method	SNR	7.3742	7.3934	7.5723
	RMSE	0.2936	0.2856	0.2804
	NCC	0.8235	0.8356	0.8734
Proposed method	SNR	12.4623	12.8476	13.1746
	RMSE	0.0782	0.0635	0.0538
	NCC	0.9362	0.9638	0.9736

5 Conclusion

To suppress periodic narrowband interference and white noise in high-voltage cable PD signals, this paper proposes a hybrid denoising method based on RIME-VMD-IWT. Based on simulation and field experiments, the main conclusions are summarized as follows:

(1) Using the RIME algorithm to adaptively optimize

the two core parameters K and α of VMD enables efficient and accurate parameter setting, avoiding the tendency of conventional optimization algorithms to fall into local optima and thereby significantly improving the accuracy of signal decomposition.

(2) Based on the CMFDE value of each IMF, the signal-dominant and noise-dominant components can be effectively identified. After the noise-dominant components are removed, IWT is applied to the signal-dominant components for secondary denoising, achieving better denoising performance than the conventional wavelet transform.

(3) Simulation and field experimental data verify that the proposed method significantly suppresses periodic narrowband interference and white noise. In terms of the three indices SNR, RMSE, and NCC, it outperforms the WOA-VMD-WT and POA-VMD-WT methods.

In summary, the proposed method efficiently removes complex noise in high-voltage cable PD signals while preserving their essential features. It offers practical application value and provides a reliable signal-processing approach for online monitoring of high-voltage cable insulation condition.

References

[1] Huo P, Li Y, Zhang Z et al (2024) Online monitoring and localization method for partial discharge of distribution cables based on pulse synchronization. High Voltage Apparatus 60(8):129-138

[2] Liu Z, Liu Z, Fan H (2018) Research on denoising of partial discharge signals of high-voltage cables based on EMD-ICA. Power System Protection and Control 46(24):83-87

[3] Huang C, Zhao Y, Hu R et al (2024) Evolution analysis of damp XLPE-SiR insulation interface discharge in 10 kV cable intermediate joints. Guangdong Electric Power 37(6):120-128

[4] Naruei I, Keynia F, Molahosseini A S (2022) Hunter-prey optimization: algorithm and applications. Soft Computing 26:1279-1314. https://doi.org/10.1007/s00500-021-06401-0

[5] Bi X, Zhong J, Zhang D et al (2021) A partial discharge denoising algorithm based on improved singular values and empirical wavelet decomposition. Power System Technology 45(12):4957-4963

[6] Sun Y, Fang Y, Zheng X et al (2024) Method for improving the automatic recognition accuracy of neural networks in online monitoring of power cable partial discharge. High Voltage Apparatus 60(7):210-220

[7] Xu X, Xu G, Wang X et al (2009) Empirical mode decomposition (EMD) and its applications. Acta Electronica Sinica 37(3):581-585

[8] Yang Y, Yu D, Cheng J (2005) Fault diagnosis method of rolling bearings based on EMD and neural networks. Journal of Vibration and Shock (1):87-90+138-139

[9] Shi J, Zhu M, Chen H et al (2020) A hydrophone signal denoising method based on VMD and wavelet threshold. Journal of Sensing Technology 33(7):1003-1012

[10] Jiang Y, Zhu Y, Yang X et al (2022) A partial discharge feature extraction method based on Hankel-SVD-CEEMDAN improved threshold. Power System Technology 46(11):4557-4567

[11] Ma X, Shi X, Zhao J (2024) MEMS denoising method based on POA-VMD-WT. Journal of Electronic Measurement and Instrumentation 38(1):53-63

[12] Zhao D, Tang X, Wang T et al (2025) Short-term photovoltaic power study based on similar-day clustering and a WOA-VMD-TCN-Transformer model. Acta Energiae Solaris Sinica 46(11):210-218

[13] Su H, Zhao D, Heidari A A et al (2023) RIME: a physics-based optimization. Neurocomputing 532:183-214. https://doi.org/10.1016/j.neucom.2023.02.010

[14] Xu X, Zhao Q, Lv G et al (2022) Research on anti-interference of GIS partial discharge monitoring based on improved wavelet threshold. Automation and Instrumentation 37(2):7-10+17

[15] Wang Y, Wang T, He J et al (2025) A partial discharge denoising method based on SVMD and improved wavelet threshold. Journal of Chongqing University of Posts and Telecommunications (Natural Science Edition) 37(4):597-606

[16] Hu B, Zhu Z, Jin F et al (2024) Fuzzy dispersion entropy and its applications. Computer Engineering and Applications 60(2):326-336

[17] Ge X, Ma H, Zhang C et al (2025) Isolation switch fault diagnosis method based on tFLO-SVMD-LSSVM and refined composite multiscale fuzzy dispersion entropy. Electric Machines and Control Application 52(4):376-388

[18] Zhang C, Fan B, Huang Y et al (2023) Experimental study and simulation analysis of partial discharge signal propagation characteristics in 10 kV power cable bodies. High Voltage Apparatus 59(1):95-101

[19] Ding Y, Wang Y, Chen M et al (2024) Study on partial discharge characteristics of high-voltage power module packaging insulation under high dV/dt square-wave voltage. Proceedings of the CSEE 44(24):9884-9897

[20] Zhou J, Luo R, Huang J (2024) A method for suppressing white noise in transformer partial discharge ultrasonic signals based on improved wavelet threshold-CEEMDAN. High Voltage Apparatus 60(1):163-171